

A Robust Motion Compensation Approach for UAV SAR Imagery

Lei Zhang, Zhijun Qiao, *Member, IEEE*, Meng-dao Xing, *Member, IEEE*,
Lei Yang, and Zheng Bao, *Senior Member, IEEE*

Abstract—Unmanned aerial vehicle (UAV) synthetic aperture radar (SAR) is an essential tool for modern remote sensing applications. Owing to its size and weight constraints, UAV is very sensitive to atmospheric turbulence that causes serious trajectory deviations. In this paper, a novel databased motion compensation (MOCO) approach is proposed for the UAV SAR imagery. The approach is implemented by a three-step process: 1) The range-invariant motion error is estimated by the weighted phase gradient autofocus (WPGA), and the nonsystematic range cell migration function is calculated from the estimate for each subaperture SAR data; 2) the retrieval of the range-dependent phase error is executed by a local maximum-likelihood WPGA algorithm; and 3) the subaperture phase errors are coherently combined to perform the MOCO for the full-aperture data. Both simulated and real-data experiments show that the proposed approach is appropriate for highly precise imaging for UAV SAR equipped with only low-accuracy inertial navigation system.

Index Terms—Local maximum-likelihood (LML), motion compensation (MOCO), phase gradient autofocus (PGA), synthetic aperture radar (SAR), unmanned aerial vehicle (UAV), weighted phase gradient autofocus (WPGA).

I. INTRODUCTION

SYNTHETIC aperture radar (SAR) is a remote sensing system to generate high-resolution microwave images of the observed scene. It is mounted on-board a platform, such as aircraft, satellite, or unmanned aerial vehicle (UAV), which flies at a constant velocity along a nominal trajectory. By transmitting wideband signals in a constant time interval, SAR can achieve the backscattering characteristics from the echoed data. As highlighted in [1], for SAR systems, the platform motion is a solution as well as a problem. The problem arises from trajectory deviations, and instability of platform velocities, which not only causes serious blurring, but also geometric distortion of the SAR imagery. Such motion errors can be obtained from the synchronous measurements of the navigation systems, and motion compensation (MOCO) is performed subsequently. To achieve highly precise MOCO, the measurements have to be performed

at subwavelength scale from pulse to pulse, which would exceed the accuracy of navigation systems. Therefore, navigation measurements usually provide only coarse MOCO, such as removal of the nonsystematic range cell migration (NRCM) and partial phase errors [2], [3]. Autofocus approaches are subsequently applied to estimate the rest motion errors. The motion error problem is particularly apparent to the UAV SAR, because it is easily disturbed by the atmospheric turbulence due to its small size and light weight. Moreover, the UAV SAR may not be equipped with a highly accurate navigation system due to weight capacity constraint [4]. Therefore, for the UAV SAR imaging, MOCO strategies are important and advisable based on the raw data.

Up to now, some raw-databased MOCO approaches have been proposed to focus the UAV SAR imagery. In [5], a MOCO strategy is proposed based on the Doppler rate (DR) estimation via the map-drift techniques [6]–[8]. It splits each subaperture data into multiple range blocks to estimate the range-varying DRs. Then, the motion errors are brought by the double integral of the DRs. The MOCO approach is performed in an iterative manner to reach an optimal accuracy. For UAV SAR imagery, it normally needs a number of iterations, resulting in large computational load. Another method presented in [9] is based on a combination of range alignment and phase gradient autofocus (PGA) [10]: The NRCM is corrected by the range alignment techniques, and the phase error is estimated by PGA. However, it also encounters the problem of huge computational load in processing large-size data, because its NRCM correction is very time consuming. In addition, the range variance of motion errors challenges the MOCO scheme in wide-swath SAR imaging. In the raw-databased approaches, autofocus techniques are employed to estimate motion errors adaptively. PGA is one of the most popular autofocus algorithms. Recent improvements in the PGA algorithms, including the quality PGA (QPGA) and the weighted phase estimation, are presented in [11]–[13], respectively. However, direct application of these novel approaches to UAV SAR imagery encounters inherent difficulties. Some factors should be accounted in the establishment of the MOCO approach for UAV SAR, which are listed as follows.

- 1) UAV SAR may not be equipped with a highly accurate navigation system. Therefore, MOCO based on raw data is essential for UAV SAR imagery.
- 2) The motion errors are serious to the UAV SAR imaging, which may not only cause phase errors, but also NRCM.
- 3) UAV usually flies at a low height, and it is required to reach a wide observation area. Thus, in the MOCO, the range variance of errors should be accounted carefully.

Manuscript received October 23, 2010; revised April 12, 2011, July 7, 2011, and September 22, 2011; accepted December 11, 2011. Date of publication February 3, 2012; date of current version July 18, 2012. This work was supported by “973” program of China under Grant 2010CB731903. The work of Z. Qiao was supported in part by the U. S. Army Research Office under Contract/Grant W911NF-08-1-0511 and by the Texas Norman Hackerman Advanced Research Program under Grant 003599-0001-2009.

L. Zhang, M. Xing, L. Yang, and Z. Bao are with National Key Lab for Radar Signal Processing, Xidian University, Xi’an 710071, China.

Z. Qiao is with the Department of Mathematics, University of Texas-Pan American, Edinburg, TX 78539-2999 USA.

Color versions of one or more of the figures in this paper are available online at <http://ieeexplore.ieee.org>.

Digital Object Identifier 10.1109/TGRS.2011.2180392

- 4) UAV SAR is required to operate under different modes, such as stripmap and spotlight mode. Therefore, its MOCO should be adjusted to these modes, particularly for the strip-map mode.
- 5) Another important factor for the MOCO of UAV SAR is the efficiency and feasibility for its real-time implementation.

Taking the aforementioned factors into consideration, we propose a robust autofocus algorithm to meet the demands of the precise and efficient MOCO for UAV SAR imagery. The core of the proposed MOCO is extending the weighted PGA (WPGA) to the range-variant case. Our approach runs a three-step estimation: 1) range-invariant motion error is estimated by the WPGA to compensate the NRCM for a subaperture data; 2) retrieval of range-dependent phase error is executed by a modified WPGA algorithm, which is precise and robust through using the weighting and local maximum-likelihood (LML) estimate, which we call LML-WPGA; and 3) all subaperture phase estimates are coherently combined into a full-aperture phase error function, and the linear phase is filtered out to prevent the image shift. In the range-variant phase estimation, the LML-WPGA is proposed by considering the fact that the spatial variance is negligible within a small range block of raw data. A novel method is also proposed to determine the range block size adaptively. By the LML, very fast convergence can be achieved and the precision of the WPGA is improved significantly. The LML-WPGA makes it suitable to correct range-variant phase errors in UAV SAR data. The algorithm can precisely be applied to the MOCO of the strip-map UAV SAR flying with a low altitude. Its extensions to other modes, such as spotlight and high squint, are also developed straightforwardly. Real UAV SAR data sets are used to test the proposed approach. Owing to its efficiency and accuracy, our approach opens the possibility for the MOCO of UAV SAR systems with equipping only a low-accuracy navigation system.

II. SIGNAL AND GEOMETRY MODEL

The UAV SAR data acquisition geometry is shown in Fig. 1, where the linear straight line (X -axis) denotes the nominal trajectory, and the curve represents the real trajectory. In the ideal case, the antenna phase center (APC) of the radar moves along the nominal path at a constant velocity V . However, owing to the displacement of real trajectory from the nominal one, additional range error from radar to target is caused. Let us assume that the pulse repetition interval is T_r . APC is located in a constant interval with the length of VT_r along the X -axis

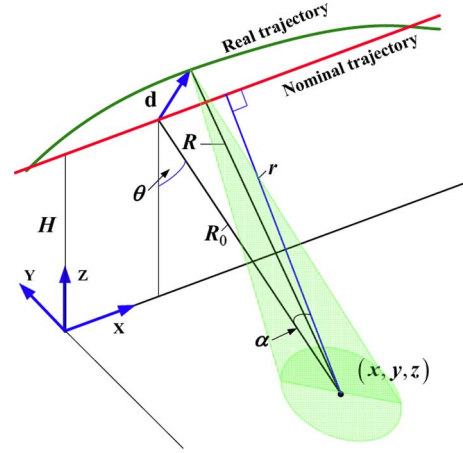


Fig. 1. UAV SAR motion geometry.

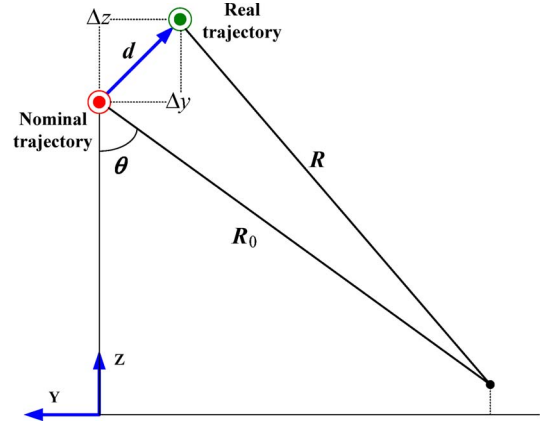


Fig. 2. Normal plane of the ideal trajectory (side-looking mode).

direction at a reference height of H . The actual and ideal APC position at the slow time t_m is $[X(t_m), \Delta y(t_m), H + \Delta z(t_m)]$ and $[Vt_m, 0, H]$, respectively. The instantaneous motion error vector d , defined by the displacement between the real and nominal trajectories, is $[\Delta x(t_m), \Delta y(t_m), \Delta z(t_m)]$, where $\Delta y(t_m)$ and $\Delta z(t_m)$ represent the cross-track displacement. Considering a scatterer at (x, y, z) and nonsquint mode ($\alpha = 0$), the instantaneous range from the actual APC to the scatterer (see (1)–(3), shown at the bottom of the page) where $r = \sqrt{y^2 + (H - z)^2}$ is the closest range of the scatterer to the ideal trajectory. Furthermore, $\sin \theta = \sqrt{1 - (H/r)^2}$ and $\cos \theta = H/r$ refers to the incidence angle, as shown in Fig. 2. In (1), the instantaneous range is approximately decomposed into two terms: R_0 corresponds to the nominal track, and ΔR stands for the range error. In (3), the first term of range error is caused

$$R(t_m; r, x) = \sqrt{(Vt_m + \Delta x(t_m) - x)^2 + (\Delta y(t_m) - y)^2 + (H + \Delta z(t_m) - z)^2} \\ = R_0(t_m; r, x) + \Delta R(t_m; x, y, z) \quad (1)$$

$$R_0(t_m; r, x) = \sqrt{r^2 + (Vt_m - x)^2} \quad (2)$$

$$\Delta R(t_m; x, y, z) \approx \frac{[2Vt_m + \Delta x(t_m) - 2x]}{2r} \cdot \Delta x(t_m) + \sin \theta \cdot \Delta y(t_m) + \cos \theta \cdot \Delta z(t_m) \quad (3)$$

by the along-track motion error, and the second and third terms are the cross-track errors. Based on the narrow beam and flat topography assumption [2], [3], [5], [14], the spatial variance of the motion error can be simplified as range dependence. Equation (3) is approximately equal to

$$\Delta R(t_m; r, x) \approx \frac{(Vt_m - x)}{r} \cdot \Delta x(t_m) + \sin \theta \cdot \Delta y(t_m) + \cos \theta \cdot \Delta z(t_m). \quad (4)$$

Suppose the radar transmits a linear frequency modulated signal

$$s_t(\hat{t}) = \text{rect} \left[\frac{\hat{t}}{T_p} \right] \exp \left[j2\pi \left(f_c \hat{t} + \frac{1}{2} \gamma \hat{t}^2 \right) \right] \quad (5)$$

where \hat{t} is the fast time, $\text{rect}[u] = \begin{cases} 1 & |u| \leq 1/2 \\ 0 & |u| > 1/2 \end{cases}$, f_c is the carrier frequency, T_p is the pulse width, and γ is the chirp rate. After down conversion to the baseband, the received signal from the scene is expressed by

$$s_r(\hat{t}, t_m) = \iint \sigma(r, x) \cdot g \left(t_m - \frac{x}{V} \right) \cdot s_t \left(\hat{t} - \frac{2R(t_m; r, x)}{c} \right) \cdot \exp \left[-j4\pi f_c \frac{R(t_m; r, x)}{c} \right] dr dx \quad (6)$$

where r and x are the range and azimuth coordinates, respectively, c is the light speed, $\sigma(r, x)$ is the complex reflectivity, and $g(t_m)$ represents the antenna pattern and other slow time-variant characters. By transforming (6) into the range frequency domain via a Fourier transform (FT), we obtain

$$\begin{aligned} s_r(f_r, t_m) &= \iint \sigma(x, r) \cdot g \left(t_m - \frac{x}{V} \right) \cdot s_t(f_r) \\ &\quad \cdot \exp \left[-j4\pi(f_c + f_r) \frac{R(t_m; r, x)}{c} \right] dr dx \\ &= \iint \sigma(x, r) \cdot g \left(t_m - \frac{x}{V} \right) \cdot s_t(f_r) \\ &\quad \cdot \exp \left[-j4\pi(f_c + f_r) \frac{R_0(t_m; r, x)}{c} \right] \\ &\quad \cdot \exp \left[-j4\pi(f_c + f_r) \frac{\Delta R(t_m; r, x)}{c} \right] dr dx \quad (7) \end{aligned}$$

where $s_t(f_r) = \mathbf{FT}[s_t(\hat{t})]$, and $\mathbf{FT}[\cdot]$ is the FT operator. The first step of conventional image formations, such as the range-Doppler algorithm [15]–[17], the chirp scaling algorithm (CSA) [3], [18]–[20], and the frequency scaling algorithm [21], is to remove the RCM caused by the ideal data acquisition geometry and the followed-up range matched filtering [1]. The signal with motion errors in the range frequency and azimuth time domain is given by

$$\begin{aligned} s_r(f_r, t_m) &= \iint \sigma(x, r) \cdot g \left(t_m - \frac{x}{V} \right) \cdot \exp \left(-j4\pi f_r \frac{r}{c} \right) \\ &\quad \cdot \exp \left[-j4\pi f_c \frac{R_0(t_m; r, x)}{c} \right] \\ &\quad \cdot \exp \left[-j4\pi f_c \frac{\Delta R(t_m; r, x)}{c} \right] \\ &\quad \cdot \exp \left[-j4\pi f_r \frac{\Delta R(t_m; r, x)}{c} \right] dr dx. \quad (8) \end{aligned}$$

The ideal RCM is deterministic and corrected precisely. However, motion errors still present phase errors and NRCM (induced by $\exp[-j4\pi f_r (\Delta R(t_m; r, x)/c)]$) when the motion error exceeds a range cell. They are expected to be corrected in the MOCO. In general, the NRCM correction requires the precise estimation of profile shift within a quarter of range cell, while the phase error correction requires higher precision, because the phase is relevant to the wavelength. In some cases where the motion error is nominal to cause NRCM, only the phase errors are taken into account. Applying the inverse FT to (8) yields the following range-compressed signal

$$\begin{aligned} s_{rc}(\hat{t}, t_m) &= \int \int \sigma(x, r) \cdot g \left(t_m - \frac{x}{V} \right) \cdot \text{sinc} \left[\gamma T_p \left(\hat{t} - \frac{2r}{c} \right) \right] \\ &\quad \cdot \exp \left[-j4\pi f_c \frac{R_0(t_m; r, x)}{c} \right] \\ &\quad \cdot \exp \left[-j4\pi f_c \frac{\Delta R(t_m; r, x)}{c} \right] dr dx. \quad (9) \end{aligned}$$

No NRCM error assumption is widely used in the current autofocus algorithms. However, in the MOCO of UAV SAR imagery, this assumption is generally too strict to apply.

III. RELATED WORKS

Before presenting our approach for the UAV SAR imagery, let us briefly review some related works.

A. Phase Gradient Autofocus and Its Improvements

The PGA is one of the useful autofocus algorithms in the SAR imagery. It provides robust performance over wide variety of scene content. By neglecting the spatial variance of phase error, PGA exploits the phase error redundancy at different range bins. Before using the PGA, the azimuth de-ramping [1], [13], [22] is applied to remove the quadratic term in $R_0(t_m; r, x)$. The de-ramping reference function for range bin at coordinate r is expressed by

$$d(t_m) = \exp \left[j2\pi \frac{(Vt_m)^2}{\lambda r} \right] \quad (10)$$

where $\lambda = c/f_c$ denotes the wavelength. Multiplying by $d(t_m)$ on both sides of (9) and by neglecting the constants and high-order phase terms, we have

$$\begin{aligned} s(\hat{t}, t_m) &\approx \int \int \sigma(x, r) \cdot g \left(t_m - \frac{x}{V} \right) \\ &\quad \cdot \text{sinc} \left[\gamma T_p \left(\hat{t} - \frac{2r}{c} \right) \right] \cdot \exp \left(j4\pi \frac{Vt_m x}{r\lambda} \right) \\ &\quad \cdot \exp \left[-j4\pi f_c \frac{\Delta R(t_m; r, x)}{c} \right] dr dx. \quad (11) \end{aligned}$$

Then, PGA is performed to estimate the phase error in (11). Standard PGA is executed in the following five steps.

—**Samples selection.** Selecting samples with high signal-to-clutter ratio (SCR) makes the estimation more efficient and precise. The QPGA extends conventional PGA by making use of the redundancy of phase error in both the range and

azimuth directions [11], which significantly increases the amount of high-quality samples by several times to obtain noniterative convergence. QPGA reveals that coherent fusion of high-quality samples is important in phase gradient estimation.

- Circular shifting.** For the selected samples, the azimuth cell with the strongest response is circularly shifted to the image center, which removes the frequency offset in the Doppler domain.
- Windowing.** Windowing processing preserves only the width of the dominant blur, which allows the phase gradient estimation to proceed using the input data with the highest SCR. The selection of window size can be obtained adaptively [10]. We also know that a progressively decreasing window width works quite well in real cases.
- Phase gradient estimate.** After circular shifting and windowing, the phase gradient is able to be estimated. Symbol $s(k, \cdot)$ is used to denote the discrete form of the k th selected range bins after circular shifting and windowing. The linear unbiased minimum variation and ML estimate kernels can be found in [8]. More recently, following the idea of weighted phase estimation in [12], a weighted ML kernel is presented in [13]. Weighting technique is based on the contribution adjustments of different samples according to their SCR, which encourages the contribution of high SCR samples in phase gradient estimate. If so, the selection of samples can be much relaxed and the fast convergence can be obtained. The weighted maximum likelihood (WML) kernel is given by

$$\hat{\phi}_e^{\text{WML}}(h) = \arg \sum_{k=1}^K \frac{w_k \cdot [\text{conj}[s(k, h)] \cdot s(k, h+1)]}{\sum_{j=1}^K w_j} \quad h = 1, 2, \dots, J \quad (12)$$

where $\hat{\phi}_e$ is the estimated phase-error gradient, K is the number of selected range bins, $J+1$ denotes the azimuth length of samples, $\text{conj}[\cdot]$ denotes the conjugate operator, and w_k is the weight in the k th range bin. The weight w_k for the k th range bin is the inverse of the phase variance of the range bin. Details can be found in [12] and [13].

- Iterative phase correction.** The phase gradient $\hat{\phi}_e$ is integrated to obtain the estimate of $\exp[-j4\pi f_c(\Delta R(t_m; r, x)/c)]$ in (11), and any bias and linear component is removed prior to performing correction. The estimation and compensation process is repeated iteratively. Prior information about the motion error, such as measurements of navigation systems, is helpful to improve the efficiency: If partial phase error can be corrected by using prior information, the initialized window width can be selected narrow enough to ensure high SCR.

B. Strip-Map Autofocus Approaches

Standard PGA framework cannot be directly applied to strip-map SAR imagery, because the apertures of different targets

displace with each other during a long observation interval in the strip-map mode. Then, applying the PGA brings a problem: Partially overlapping apertures, which span different segments of the phase error function with potentially different local linear components, will not necessarily express the same phase gradients in the overlapped region [23]. To solve this problem, the phase curvature autofocus (PCA) has been proposed in [23]. However, owing to the double differentiation characteristics, PCA is inherently less robust than PGA [24]. The SCR weighting process can effectively improve the performance of PCA [13], [24]. The strip-map PGA [25] and the phase-matching autofocus [26] present modifications by combining the Doppler centroid estimation [27]–[29]. All these strip-map autofocus algorithms do not have the spatial variance of motion errors involved. The phase-weighted-estimation PGA (PWE-PGA) [30] provides a weighted kernel with a range-variant model for strip-map data. It computes the phase gradients other than the phase curvatures by converting data blocks of the strip-map SAR into the spotlight representation. In PWE-PGA, the trajectory derivation caused by the along-track motion error is neglected, and there are only the cross-track motion errors. According to the geometry shown in Fig. 2, the instantaneous range error (4) is approximated by

$$\Delta R(t_m; r) \approx \sin \theta \cdot \Delta y(t_m) + \cos \theta \cdot \Delta z(t_m) \quad (13)$$

This range-variant model decomposes the phase error ϕ_e into a vertical and a horizontal part, denoted by $\phi_{ez} = (4\pi/\lambda)\Delta z$ and $\phi_{ey} = (4\pi/\lambda)\Delta y$, respectively, corresponding to the geometry shown in Fig. 2. The phase gradient estimation of PWE-PGA is

$$\hat{\Phi}_{yz} = (\mathbf{A}^T \mathbf{W} \mathbf{A})^{-1} \mathbf{A}^T \mathbf{W} \hat{\Phi} \quad (14)$$

where $[\cdot]^T$ and $[\cdot]^{-1}$ denotes matrix transpose and inverse, respectively. $\mathbf{A} = \begin{bmatrix} \sin \theta_1 & \cos \theta_1 \\ \vdots & \vdots \\ \sin \theta_K & \cos \theta_K \end{bmatrix}$

and $\mathbf{W} = \text{diag}[m_1, \dots, m_K]$ are the geometry and weighting matrix, respectively, with $\sin \theta_1$, $\cos \theta_1$ and $m_k = \sum_{h=1}^J |[\text{conj}[s(k, h)] \cdot s(k, h+1)]|$ corresponding

to the k th range bin sample, and $\hat{\Phi} = \begin{bmatrix} \hat{\phi}_e(1, \cdot) \\ \vdots \\ \hat{\phi}_e(K, \cdot) \end{bmatrix}$

is the estimated phase gradient matrix with $\hat{\phi}_e(k, h) = \arg[\text{conj}[s(k, h)] \cdot s(k, h+1)]$, $k = 1, 2, \dots, K$, $\hat{\Phi}_{yz} = \begin{bmatrix} \hat{\phi}_{ey} \\ \hat{\phi}_{ez} \end{bmatrix}$ being the matrix for the cross-track phase gradients estimate.

$\hat{\phi}_{ey}$ and $\hat{\phi}_{ez}$ represent the phase gradient estimation related to $\Delta y(t_m)$ and $\Delta z(t_m)$, respectively. The weights in PWE-PGA are determined by energy, which can be replaced by the SCR weights to improve the performance [13], [24]. PWE-PGA paves a way to autofocus SAR image with a wide swath and low altitude. However, some difficulties in application of PWE-PGA to the UAV SAR imagery make it unsuitable candidate for the raw-database MOCO. In (14), we need to retrieve 2-D

phase gradients rather than the 1-D case in PGA from a set of inaccurate phase gradient related to a range bin. Consequently, to ensure the precise estimation and convergence of PWE-PGA, more range samples are needed, which restricts the PWE-PGA application to different scenes because some scenes may not have enough prominent scatterers. Phase gradients of different range bins are affected by strong noise, and they are not coherently combined into high-accuracy estimates. Direct usage of the noisy phase gradients in the PWE-PGA kernel causes imprecision of $\hat{\Phi}_{yz}$, which results in a very slow convergence. In addition, in addition to neglecting the along-track motion error, another problem in the PWE-PGA is the phase discontinuities between the blocks. In summary, the PWE-PGA is not an efficient and robust approach to satisfy the application of the UAV SAR imagery, where serious motion error and the uncertainty of observation scene are usually involved. This motivated our work presented in this paper.

IV. UAV SAR AUTOFOCUS APPROACH

In this section, we present a robust autofocus algorithm for the UAV SAR imagery. It accounts both the phase error and NRCM. Furthermore, the approach applies the range-variant error model, and thus it is suitable to process strip-map SAR data. Similar to the PWE-PGA, it could be directly applied to the spotlight and high squint case with some modifications. The phase errors estimation is composed of the following three main steps in our approach to the UAV SAR MOCO based on raw data.

- 1) First, the UAV SAR raw data is divided into several overlapped small subapertures to deal with the uncertainty of linear phase component in the PGA application of strip-map SAR autofocus. The range-invariant phase errors for each subaperture data are estimated by the WPGA, and then coarse MOCO is performed on the data block, including NRCM correction and range-invariant phase error removal. At this step, the coarse information from the navigation system, if available, is useful.
- 2) After the coarse MOCO in the first step, NRCM can be corrected effectively. Residual phase errors are range variant, usually only being a fraction of the total errors, but significantly enough to cause image blurring. In the range-variant error estimation, a LML scheme is proposed to ensure the robustness and high precision.
- 3) At this step, the estimated subaperture phase errors are coherently combined into full-aperture phase functions. As each sub-aperture error estimate is independent of each other, different linear phases are involved in each sub-aperture. Therefore, the overlapping between two connective subapertures is necessary, and the linear phase difference is easily extracted from the overlapped segments and compensated to avoid discontinuities in the full-aperture functions. This procedure is processed for both range-invariant and range-variant phase errors. Then, the smoothing filter is applied to reduce the estimating noise. Based on the full-aperture phase errors, precise MOCO can be performed by a two-step procedure.

A. Coarse Phase Estimation

Through the course of a synthetic aperture, as the radar's perspective changes toward a target, the ranges to the target change as well, which leads to the geometry-related RCM. This RCM is removed within the image formation process. In this paper, we use the CSA. Notably, image formation compensates the RCM from the acquisition geometry, but not that from motion errors. As a result, the motion errors still manifest themselves as both NRCM and phase error in the data. For the UAV SAR systems, however, the NRCM is approximately identical in different parts of the SAR image, that is, NRCM is range independent. This approximation is rigid because even in the case of wide swath UAV SAR imagery, the range-variant part of NRCM cannot exceed a range cell. This allows us to estimate the NRCM from the range-invariant phase error. By integrating the phase gradient $\hat{\phi}_{ec}(t_m)$, we obtain the phase error estimate, denoted by $\hat{\phi}_{ec}(t_m)$, and the range error can be deduced from $\hat{\phi}_{ec}$, which is expressed by

$$\Delta\hat{R}(t_m) \approx \frac{c}{4\pi f_c} \cdot \hat{\phi}_{ec}(t_m). \quad (15)$$

Then, the coarse correction function to remove range-invariant phase error and the NRCM is given by

$$G_1(t_m) = \exp \left[j4\pi(f_r + f_c) \frac{\Delta\hat{R}(t_m)}{c} \right]. \quad (16)$$

The presence of NRCM degrades the precision of the WPGA estimate of $\hat{\phi}_{ec}(t_m)$. We can perform the WPGA to the raw data with a lower resolution by the downsampling process. The downsampling process eliminates NRCM by summing up several neighboring range bins into a single bin. Also, the processing can be implemented by extracting only a part of the frequency band from the raw data to obtain the range-compressed data block [31], which inherently has an energy loss of the signal. Therefore, the summing process should be preferable. The amount of adjacent range bins to combine should cover the range of NRCM, and the price of SCR loss is usually nominal. The span of NRCM could be estimated from a coarse phase error. To avoid high computational load, the coarse phase error can be extracted from only a part of the samples. At this step, the coarse phase error estimate exhibits little difference from the conventional WPGA with regard to the spotlight SAR imagery, except the inclusion of the downsampling process.

B. Fine Phase Estimation

The task of fine phase estimation is to retrieve the range-variant error phase accurately. In PWE-PAG, the range-dependent error model only deals with the cross-track trajectory deviations. For the UAV SAR, serious along-track deviation may also bring significant phase errors. In this paper, we have developed a new range-dependent motion error model. After

the NRCM correction and coarse phase compensation, the de-ramped signal becomes

$$s(\hat{t}, t_m) = \iint \sigma(x, r) \cdot g\left(t_m - \frac{x}{V}\right) \cdot \text{sinc}\left[\gamma T_p \left(\hat{t} - \frac{2r}{c}\right)\right] \cdot \exp\left(j4\pi \frac{V t_m x}{r\lambda}\right) \cdot \exp\left[-j4\pi f_c \frac{\Delta R'(t_m; r, x)}{c}\right] dr dx \quad (17)$$

where $\Delta R'(t_m; r) = \Delta R(t_m; r) - \Delta \hat{R}(t_m)$ is the range-dependent residual range error. In general, the coarse phase correction removes major phase error in the signal, and a coarse-focused image is achieved. Therefore, the coarse phase correction is very helpful for the range sample selection and iterative phase gradient estimation, which benefits the range-dependent phase error retrieval in this step. Based on the narrow beam and flat topography assumption, the residual phase error is range dependent, which is expanded into Taylor series with respect to range as follows:

$$\Delta R'(t_m; r, x) \approx \frac{c}{4\pi f_c} \cdot [\theta_0(t_m) + \theta_1(t_m)\Delta r + \theta_2(t_m)\Delta r^2] \quad (18)$$

where $\Delta r = r - r_c$, r_c is the closet distance from the scene center to the ideal track, the first term in the bracket is the residual range-invariant error, and the second and third terms are linear and quadratic range-variant error, respectively. Unlike the range-dependent model in (13), in (18), the range dependence of motion error does not correspond to the data acquisition geometry. This range-variant model is capable of containing any kinds of range-dependent errors, including both along-track and cross-track derivations. Generally, the second-order Taylor series expansion is precisely enough to represent the range dependence of motion error.

Adapting both WPGA and PWE-PGA, the phase gradient estimate kernel for our range-variant error model is developed as

$$\hat{\boldsymbol{\vartheta}} = (\mathbf{A}^T \mathbf{M} \mathbf{A})^{-1} \mathbf{A}^T \mathbf{M} \hat{\boldsymbol{\Omega}} \quad (19)$$

where $\mathbf{A} = \begin{bmatrix} 1 & \Delta r(1) & (\Delta r(1))^2 \\ \vdots & \vdots & \vdots \\ 1 & \Delta r(K) & (\Delta r(K))^2 \end{bmatrix}_{K \times 3}$, and

$\mathbf{M} = \text{diag}[m_1, \dots, m_K]_{K \times K}$ is the weighting matrix with m_k , which denotes the inverse of the phase variance for the k th

range bin, $\hat{\boldsymbol{\Omega}} = \begin{bmatrix} \hat{\phi}'_e(1, :) \\ \vdots \\ \hat{\phi}'_e(K, :) \end{bmatrix}_{K \times J}$ is the phase gradient estimate

matrix with being $\hat{\phi}'_e(k, :)$, the residual phase gradient vector of the k th range bin, and $\hat{\boldsymbol{\vartheta}} = \begin{bmatrix} \hat{\theta}_0(:) \\ \hat{\theta}_1(:) \\ \hat{\theta}_2(:) \end{bmatrix}_{3 \times J}$ is the estimate

matrix for the polynomial phase gradient. $\hat{\theta}_0(:)$, $\hat{\theta}_1(:)$, and $\hat{\theta}_2(:)$ represent the vector of the phase gradient of range-invariant, the first-order, and second-order phase gradient term, respectively. As described earlier, $J + 1$ still stands for the azimuth length of

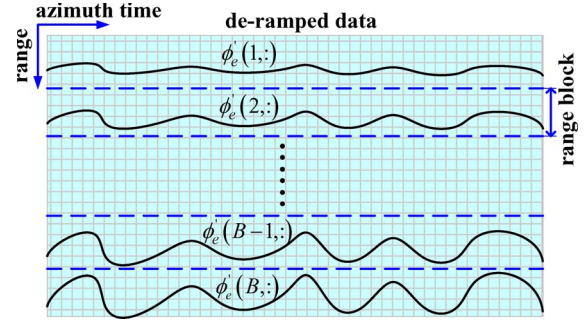


Fig. 3. Range variance and local range invariance of phase errors.

the data. Similar to PWE-PGA, the polynomial phase gradient estimate kernel has problem in the precision and efficiency. Direct application of the polynomial phase gradient kernel may require a large amount of range samples. Moreover, as the gradient phase of each range bin is interfered by strong noise, the precision and efficiency of this kernel is not ensured, even if we use the SCR weighting.

One can easily understand that in the polynomial phase gradient estimate kernel, if each range bin provides an accurate estimation of the phase gradient, high precision, and fast convergence are achievable. The robustness of the WPGA lies in the coherent fusion process, such that it coherently combines different range samples overcoming the estimating noise in the phase gradients. In UAV SAR imaging, although the motion error presents strong range variance along the whole swath, it is approximately invariant within a small range block, that is, residual phase presents a local range invariance. Another factor that we want to stress in the range-dependent phase error estimate is that the range bins, distributing over a wide extent, should be selected to provide sufficient range-variant information, which is different from the selection scheme in the standard PGA. Considering the local range invariance, we make some significant improvements to the phase gradient estimation kernel in (19). First, the de-ramped data are split into B blocks in range, as shown in Fig. 3. Each block is expected to provide an invariant phase gradient $\hat{\phi}'_e(b, :)$ with high precision by coherently combining the estimates from selected G range bins within the block

$$\hat{\phi}'_e(b, h) = \arg \sum_{g=1}^G \frac{m_{b,g} \cdot [\text{conj}[s_b(g, h)] \cdot s_b(g, h + 1)]}{\sum_{j=1}^G m_{b,j}} \quad (20)$$

where $m_{b,g}$ denotes the SCR weight of the g th sample bin in the b th range block data (referred to as $s_b(g, :)$). For the b th range block, the weight w_b is given by

$$w_b = \sum_{g=1}^G m_{b,g}. \quad (21)$$

The synthetic range corresponding to the b th range block is calculated by

$$\Delta \bar{r}_b = \sum_{g=1}^G \frac{\Delta r_b(g) \cdot m_{b,g}}{w_b}. \quad (22)$$

Then, the estimate kernel in (19) becomes

$$\hat{\vartheta} = (\mathbf{A}_{block}^T \mathbf{W} \mathbf{A}_{block})^{-1} \mathbf{A}_{block}^T \mathbf{W} \hat{\Omega} \quad (23)$$

where

$$\mathbf{A}_{block} = \begin{bmatrix} 1 & \Delta\bar{r}_1 & (\Delta\bar{r}_1)^2 \\ \vdots & \vdots & \vdots \\ 1 & \Delta\bar{r}_B & (\Delta\bar{r}_B)^2 \end{bmatrix}_{B \times 3} \quad (24)$$

$$\hat{\Omega} = \begin{bmatrix} \hat{\phi}'_e(1, :) \\ \vdots \\ \hat{\phi}'_e(B, :) \end{bmatrix}. \quad (25)$$

This phase gradient estimate kernel is developed by applying the local range invariance of phase error. Therefore, we call it the LML-WPGA kernel.

For the clarity of the LML-WPGA for range-variant phase estimation, we have employed a feasible procedure as follows:

- **Selecting samples for each range block.** This step is similar to the procedure in the conventional PGA. However, as we split the data into small blocks in range, each block may only contain a few good range bins with prominent scattering centers. To increase the amount of useful samples, the phase error redundancy in azimuth should also be used similar to the QPGA, at a price of increasing computational load. In this step, the weights and the matrix \mathbf{A}_{block} are also calculated.
- **Circular shifting.** It is used to move the azimuth cell with the strongest response to the image center for each block data.
- **Windowing.** In our approach, this processing is a little different from the one in the standard PGA, because the phase errors in different range blocks have different values causing distinct degrees of blurring. Therefore, the window width for each range block should be determined separately.
- **Phase gradient estimation.** Estimation is performed independently to each range block data by the WML kernel. As the phase gradient information of different range bins are coherently fused, the precise estimation of phase gradient is achieved for each range block.
- **LML-WPGA estimation.** This is applied to provide the estimation of the polynomial phase gradients. Clearly, in LML-WPGA, the dimension of matrix $\mathbf{A}_{block}^T \mathbf{W} \mathbf{A}_{block}$ corresponds to the number of range blocks, rather than the quantity of the range bins. For example, if we break the data into 32 blocks in range, then the size of the matrix \mathbf{A}_{block} is only 32×3 . Thus, the nominal computational load is involved in calculating matrix multiplication and inverse of $\mathbf{A}_{block}^T \mathbf{W} \mathbf{A}_{block}$. Accurate polynomial phase gradients are estimated by the weighting and LML estimate. In the following subsection, one can note that LML-WPGA requires much less iterations to reach a precise estimate than conventional methods, which indicates high efficiency of LML-WPGA.

Similar to the standard PGA, our approach utilizes an iterative phase correction and estimation scheme. The estimated polynomial phase gradient $\hat{\theta}_0$, $\hat{\theta}_1$ and $\hat{\theta}_2$ are integrated to obtain

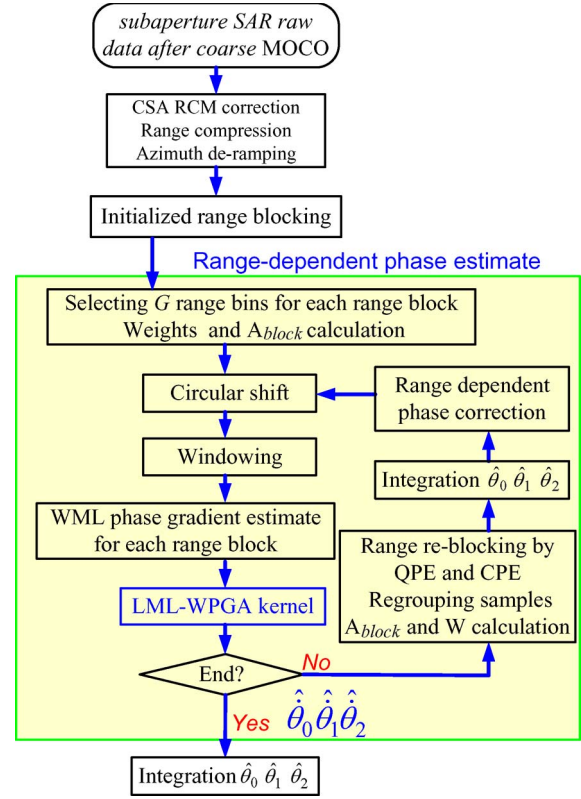


Fig. 4. LML-WPGA flowchart.

the estimate of θ_0 , θ_1 and θ_2 . For each range bin, the correction phase function is calculated by using (18). Then, range-variant phase correction is performed to the de-ramped data. Both estimation and correction are repeated iteratively. In the procedure, the high accuracy of block phase gradients provides a very fast convergence of the algorithm. Only after several iterations, accurate polynomial phase gradients are estimated by the LML-WPGA kernel. As the major part of phase errors is compensated in the coarse correction procedure, at this step, the window width can be initialized as narrow as possible, accelerating the convergence dramatically. Furthermore, to promote the efficiency of LML-WPGA, the captured scatterers are zero padded into a short vector (such as 64 points [11]) for phase gradients estimate, and we interpolate the estimates into full-aperture length in the range-dependent phase correction step.

Now, the following question arises: How to determine the size of range block to ensure the range invariance of phase errors within individual range blocks. Clearly, the magnitude of residual phase error should be accounted in the blocking. In the case where phase error expresses severe range variance, small range segmentation should be applied to eliminate estimate error within an individual block. Conversely, the block can be relatively large in small phase error case, which usually promotes both the precision and efficiency of the LML-WPGA. Without increasing additional computational load and complexity, the range blocking has been embedded into the iterative procedure of the phase gradient estimate kernel. Setting B range blocks as initialization, the range variance of phase error can be extracted from $\hat{\theta}_1$, and $\hat{\theta}_2$. In the following iteration, adaptive range segmentation is performed for the subsequent

iteration by using $\hat{\theta}_1$, and $\hat{\theta}_2$. As $\hat{\theta}_1$ usually contains most of the range variance information of the residual phase, we can consider only $\hat{\theta}_1$. Generally, for a short duration of time, higher order terms usually take fraction of $\hat{\theta}_1$, and hence, the quadratic and cubic components can be applied to determine the range block size. First, the phase gradient vector $\hat{\theta}_1/2\pi$ is fitted into a cubic function with respect to the slow time, and the linear and quadratic coefficients are denoted by μ_1 and μ_2 , which correspond to the quadratic and cubic coefficients of phase error $\hat{\theta}_1$, respectively. Then, the quadratic phase error (QPE) and cubic phase error (CPE) [1] between two range gates distanced by ΔD are defined by

$$\text{QPE} = \pi\mu_1 \cdot \Delta D \cdot \left(\frac{T}{2}\right)^2 \quad \text{CPE} = \frac{1}{3}\pi\mu_2 \cdot \Delta D \cdot T^3 \quad (26)$$

where T denotes the time duration of the subaperture. To ensure the range invariance of a range block with size ΔD , both QPE and CPE magnitudes are constrained to be less than $\pi/4$. Therefore, the range block size can be determined by $\Delta D = \min[1/\mu_1 T^2, 3/4\mu_2 T^3]$. In strip-map data processing, we usually divide received data into several subapertures, and subsequently we have relatively large ΔD . Also, high-order turbulence of phase error would be avoided during a short interval, which makes the blocking rule valid to apply. Before going to the next iteration of LML-WPGA, the samples collected are regrouped into range blocks with size ΔD . The range block number B , matrix \mathbf{A}_{block} and weights are also updated correspondingly. The adaptive segmentation only involves the linear fitting processing, which increases little computational load. Furthermore, it reduces model error from the range-invariance approximation blocking processing and also effectively promotes the convergence of LML-WPGA in the medium- and small-phase error cases. We have presented the flowchart of the LML-WPGA in Fig. 4. Clearly, when compared with WPGA, the LML-WPGA has some additional calculations, such as the matrix multiplication, matrix inverse, and the range-blocking processing. However, the computational load of LML-WPGA is just a little bit more than WPGA. We also found that decreasing the block size through increasing the iteration number is able to promote the accuracy of LML-WPGA effectively.

In our MOCO of UAV SAR imagery, the LML-WPGA is used as a subprocess to estimate the range-variant part of phase errors. However, the LML-WPGA approach is ready to autofocus the spotlight SAR image without any modification. To demonstrate the performance and effectiveness of the LML-WPGA with regard to autofocusing the SAR image, we performed experiments with the SAR data from the website of Sandia Lab (<http://www.sandia.gov/radar/sar-data.html>). We added range-variant motion errors into the data in the range-compressed and azimuth time domain according to the geometry shown in Fig. 1. The phase errors in X -, Y - and Z -axis are set as a tenth-order polynomial function given in Fig. 5. The platform height is assumed to be 3000 m, and the closest distance from the scene center to the nominal trajectory is set as 15 000 m. The range bin width of the image and wavelength are supposed to be 1 and 0.03 m, respectively. According to

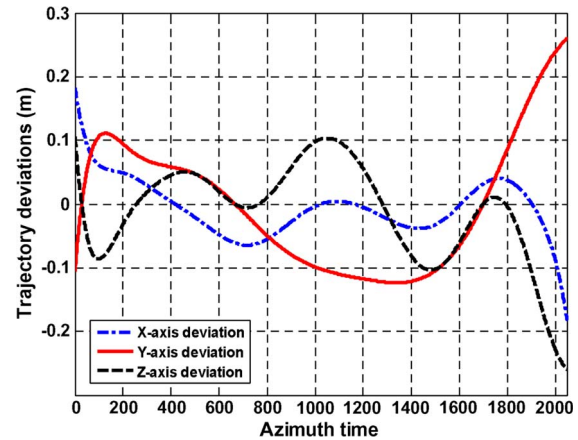


Fig. 5. Trajectory deviations.

these parameters, the range-variance phase error for each range bin can easily be calculated and added to the SAR data. All experiments in this paper were run on a personal computer with Core 2.53 GHz CPU with MATLAB.7.0.1.

Herein, the experiment was performed to validate the effectiveness of LML-WPGA for range-variant phase autofocus. In the experiment, we compared the proposed method to conventional WPGA. The mean-squared error (MSE) [11] between the added and estimated phase errors was used as a performance measurement metric. Both WPGA and LML-WPGA were used to focus the image. To present the robustness of both WPGA and LML-WPGA, the tested SAR image was about a plain scene, and only a few range bins contained prominent scatterers. In terms of evaluating the focusing performance, the image entropy was calculated. Small entropy indicates optimal focusing quality. The original SAR image is shown in Fig. 6(a) with entropy 14.92. By adding range-variant phase errors, the blurred image was generated, as shown in Fig. 6(b), and its entropy was up to 15. The WPGA was applied to refocus the image. As the range-invariant phase error plays a dominant role in the total error, the WPGA removed significant phase errors, and a focused image was generated, as shown in Fig. 6(c). However, the range-variant part of phase error was left and resulted in some blurring, particularly in the range boundary of the scene. In the processing of LML-WPGA to the blurring image, the data was blocked into 16 segments in the range initially, and each range block gave a phase gradient estimate independently. The regenerated image from the LML-WPGA is presented in Fig. 6(d). Apparently, the LML-WPGA was able to estimate both range-invariant and variant phase errors, and a better focused performance was achieved. It should be emphasized that only 128 samples were selected by their contrasts in the range-compressed and azimuth time domain [11], and they were applied in both WPGA and LML-WPGA in this experiment. Moreover, identical predetermined windowing scheme was adopted in terms of equality of the comparison. The original window width was 400, and it decreases by 30% for the subsequent iteration. The WPGA utilized about 14.1 s, increased up to about 14.4 s in LML-WPGA due to additional calculation. Fig. 6(e) and (f) presents the local images on the range boundary. One may view the residual blurring of a prominent scatterer in the WPGA result, while in the

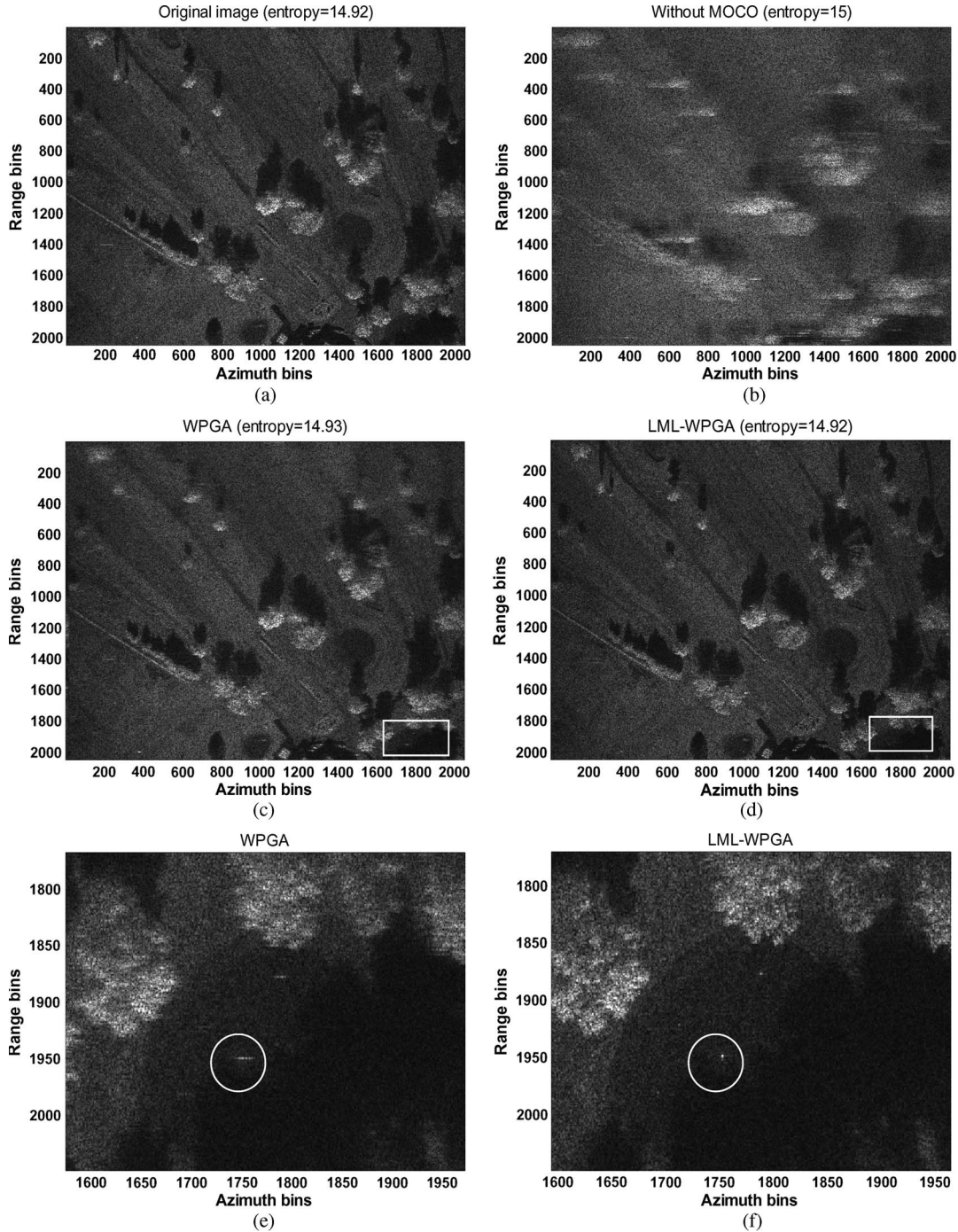


Fig. 6. Performance test of the WPGA and LML-WPGA. (a) Original image. (b) Defocused image. (c) Refocused image by the WPGA. (d) Refocused image by the LML-WPGA. (e) Local image by the WPGA. (f) Local image by the LML-WPGA.

LML-WPAG image, the scatterer is focused ideally. To evaluate the estimate precision quantitatively, in Fig. 7, we have given the difference between the added and WPGA, and LML-WPGA estimated phase errors corresponding to three different range gates (256, 1024, and 1986). The MSEs between the added and estimated phases were also calculated, which are given in Fig. 7. Although the WPGA could remove most of the range-independent phase errors, the residual range-variant parts were still in the order of several radians, which were significant enough to cause blurring. The LML-WPGA removed the entire phase errors ideally with only about five iterations effectively.

C. Extending LML to WPCA and PWE-PGA

The fast convergence and high precision of the LML-WPGA lie in the utilization of the local spatial-invariance of the phase error. In each iteration, the phase gradients of neighboring samples are fused coherently, and precise phase gradient estimate is provided for a individual block. These lead to accurate estimation at the beginning iterations of the LML-WPGA. In this subsection, following motion error model in (13), we have extended this idea to PWE-PGA and WPCA [13] in terms of improvement of accuracy and efficiency. Both PWE-PGA and WPCA are constructed based on the error model, where

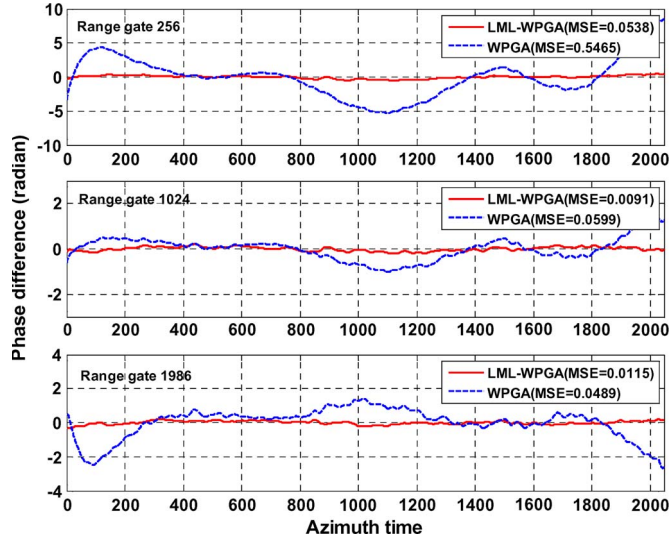


Fig. 7. Differences and MSEs between added and estimated phase errors.

the motion error is decomposed into horizontal and vertical components that vary with the looking angle. By assuming that there are K samples selected, we have grouped the samples into B blocks, within which the samples are adjacent in looking angles (assuming that each block contains G samples and that phase errors are approximately identical). For the b th block, the phase gradient $\hat{\phi}'_e(b, :)$ is estimated by the WPGA, and the synthetic looking angle, corresponding to the b th range block, is calculated by

$$\bar{\theta}_b = \sum_{g=1}^G \frac{\theta_b(g) \cdot m_{b,g}}{w_b} \quad (27)$$

where $\theta_b(g)$ denotes the incident angle corresponding to the g th sample in the b th block. By redefining the spatial variance

$$\mathbf{A}_{block} = \begin{bmatrix} \sin \bar{\theta}_1 & \cos \bar{\theta}_1 \\ \vdots & \vdots \\ \sin \bar{\theta}_B & \cos \bar{\theta}_B \end{bmatrix}_{B \times 3}, \quad \text{we can refine the}$$

PWE-PGA and WPCA kernels as

$$\begin{aligned} \hat{\Phi}_{yz} &= (\mathbf{A}_{block}^T \mathbf{W} \mathbf{A}_{block})^{-1} \mathbf{A}_{block}^T \mathbf{W} \hat{\Omega} \\ \hat{\Phi}_{yz} &= (\mathbf{A}_{block}^T \mathbf{W} \mathbf{A}_{block})^{-1} \mathbf{A}_{block}^T \mathbf{W} \hat{\Omega} \end{aligned} \quad (28)$$

where $\hat{\Phi}_{yz} = \begin{bmatrix} \hat{\phi}'_{ey} \\ \hat{\phi}'_{ez} \end{bmatrix}$ corresponds to the horizontal and vertical

phase curvature of phase errors. $\hat{\Omega} = \begin{bmatrix} \hat{\phi}'_e(1, :) \\ \vdots \\ \hat{\phi}'_e(B, :) \end{bmatrix}$, and $\hat{\phi}'_e(b, :)$

is the estimated phase double difference corresponding to b th block and can be estimated by the SCR weighted ML kernel [13].

$$\begin{aligned} \hat{\phi}'_e(b, h) &= \arg \sum_{g=1}^G \frac{m_{b,g} \cdot [s_b(g, h-1) \cdot \text{conj}[s_b(g, h)]^2 \cdot s_b(g, h+1)]}{\sum_{j=1}^G m_{b,j}} \end{aligned} \quad (29)$$

In single iteration, the computational burden of LML-PWE-PGA and LML-WPCA is nearly equal to that of PWE-PGA and WPCA. However, accommodated by the LML, both WPCA and PWE-PGA can be improved promisingly in both efficiency and precision.

In the LML-WPGA, we have developed an adaptive blocking scheme. Herein, QPE and CPE are also employed to determine the angle size of the block. Considering the angle range $\Delta\theta$ of a block around center angle θ , we have the QPE and CPE as follows:

$$\begin{aligned} \text{QPE} &= \pi \cdot \{[\sin(\theta + \Delta\theta) - \sin \theta] \mu_{y1} \\ &\quad + [\cos(\theta + \Delta\theta) - \cos \theta] \mu_{z1}\} \cdot \left(\frac{T}{2}\right)^2 \\ \text{CPE} &= \frac{1}{3} \pi \{[\sin(\theta + \Delta\theta) - \sin \theta] \mu_{y2} \\ &\quad + [\cos(\theta + \Delta\theta) - \cos \theta] \mu_{z2}\} \cdot T^3 \end{aligned} \quad (30)$$

where μ_{y1} and μ_{z1} represent the quadratic coefficients of $\hat{\phi}'_{ey}/2\pi$ and $\hat{\phi}'_{ez}/2\pi$, respectively, and μ_{y2} and μ_{z2} are the cubic coefficients, respectively. They can be retrieved by polynomial fitting. Based on approximations $\Delta\theta \ll \theta$ and $\sin(\Delta\theta/2) \approx \Delta\theta/2$, we have

$$\begin{aligned} \text{QPE} &\approx \pi \Delta\theta \cdot (\cos \theta \mu_{y1} - \sin \theta \mu_{z1}) \cdot \left(\frac{T}{2}\right)^2 \\ \text{CPE} &\approx \frac{1}{3} \pi \Delta\theta \cdot (\cos \theta \mu_{y2} - \sin \theta \mu_{z2}) \cdot T^3 \end{aligned} \quad (31)$$

Both QPE and CPE magnitudes should be restricted within $\pi/4$. Therefore, the block size around incidence angle θ can be determined by $\Delta\theta = \min[1/(\cos \theta \mu_{y1} - \sin \theta \mu_{z1})T^2, 3/4(\cos \theta \mu_{y2} - \sin \theta \mu_{z2})T^3]$.

To investigate the performance enhancement of both PWE-PGA and WPCA using the LML scheme, we performed experiments by employing the Sandia's SAR data. In the experiment, motion errors only in Y - and Z -axis were added into the range-compressed data. LML-PWE-PGA and LML-WPCA, together with the original PWE-PGA and WPCA, were applied to refocus the image. Their performance was evaluated by MSE between the added and estimated phase errors at the three range gates. In the experiment, improvements on convergence and precision by LML were tested. The same 256 samples with largest contrast were used in all algorithms. Identical predetermined windowing scheme was adopted for the purpose of equality. The original window width is 400, which decreased by 30% for the subsequent iteration. The total iteration number was 15. The consuming time of WPCA, PWE-PGA, LML-WPCA, and LML-PWE-PGA was 25.44, 20.26, 25.81 and 20.43 seconds, respectively. The image results of WPCA, PWE-PGA, LML-WPCA, and LML-PWE-PGA are shown in Fig. 8. Their image entropies were 14.94, 14.94, 14.92, and 14.92, respectively, exhibiting significant focusing enhancement by the LML processing. Because of low SCR of the samples and scarcity of prominent scatterers of the data, both original WPCA and PWE-PGA involved strong noise in the estimate,

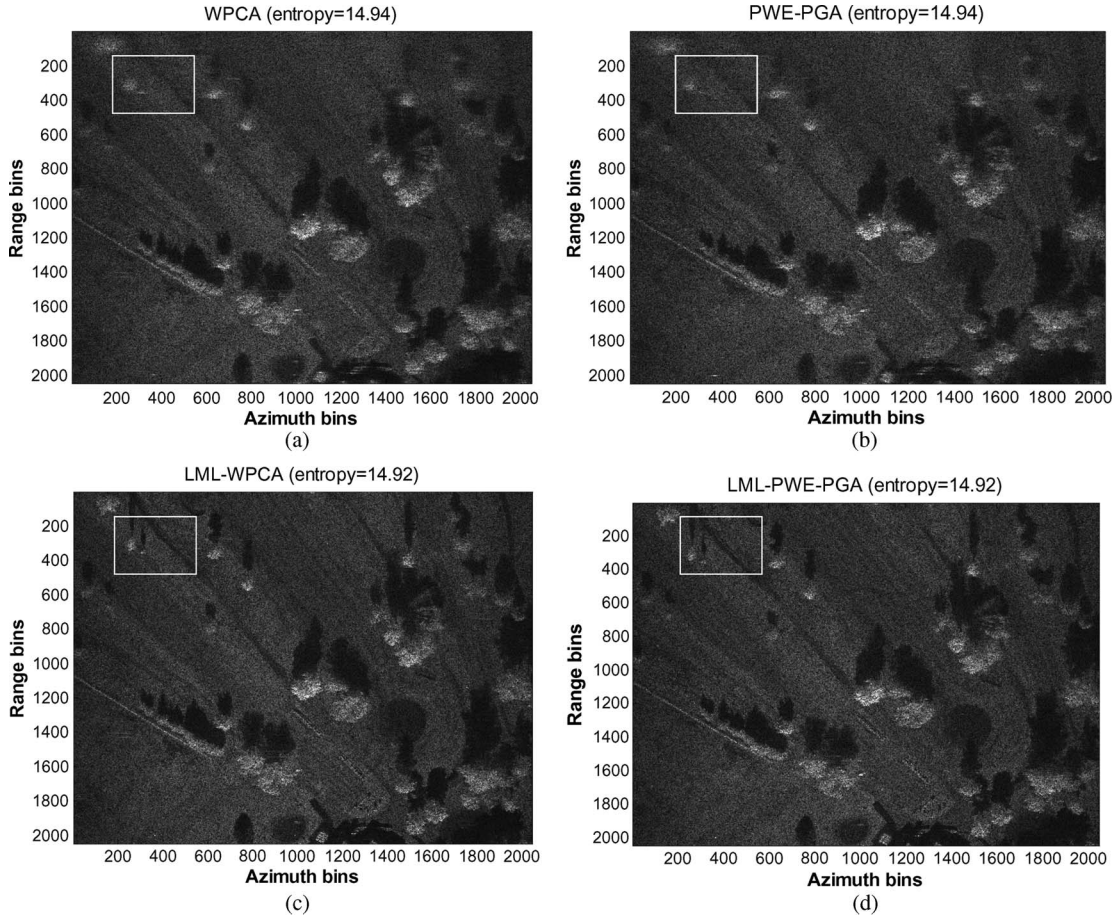


Fig. 8. Image results from the conventional and LML-based autofocus algorithms. (a) WPCA result. (b) PWE-PGA result. (c) LML-WPCA result. (d) LML-PWE-PGA result.

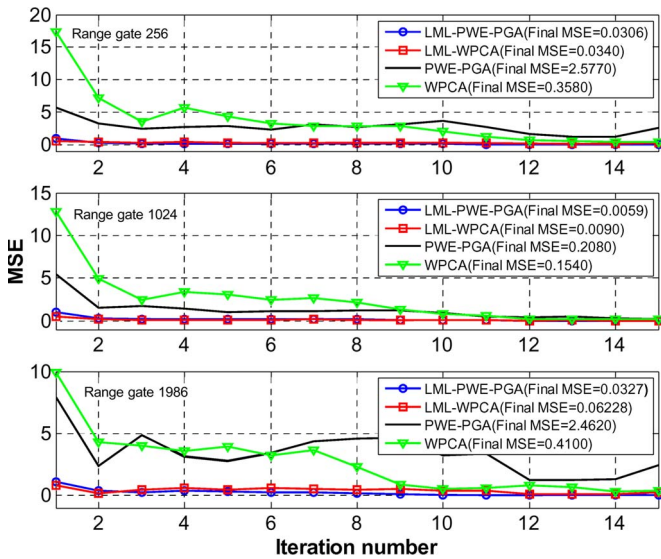


Fig. 9. Convergence of conventional and LML-based autofocus algorithms.

which led to significant blurring in the image. Nevertheless, in LML-WPCA and LML-PWE-PGA images, high-quality focusing was achieved all over the scene and exhibiting promising precision improvement. We analyzed the convergence of the algorithms by plotting the MSE change with the iteration number corresponding to the three range gates (Fig. 9). Owing

to the strong noise interference in single bin estimate, both WPCA and PWE-PGA were found to provide very coarse estimates in the beginning iterations. As the iteration number increased, their MSEs changed slowly and maintained a relatively high level. However, both LML-WPCA and LML-PWE-PGA achieved much lower MSE curves than the original kernels. LML-WPCA and LML-PWE-PGA provided nearly noniterative convergence, because their estimates were very precise at the beginning iteration, and converged to an optimal value after a few iterations. High precision and fast convergence from the LML processing ensured high efficiency of LML-WPCA and LML-PWE-PGA, because we only used several iterations to implement them without losing accuracy. We also found that the LML-based methods perform robustly when only 128 samples were used. However, in this case, neither WPCA nor PWE-PGA could generate focused image. Clearly, enhanced by the LML processing, promising improvement could be achieved for both WPCA and PWE-PGA. Furthermore, based on the geometric error model and no assumption of beam center approximation [32], both PWE-PGA and WPCA were found to be ready to be accommodated in the topography- and aperture-dependent MOCO [33]–[35] by using an external digital elevation model. Owing to the efficiency and accuracy improvement following LML processing, they can achieve better performance in many radar imaging activities, such as residual motion removal in airborne repeat-pass SAR interferometry [13].

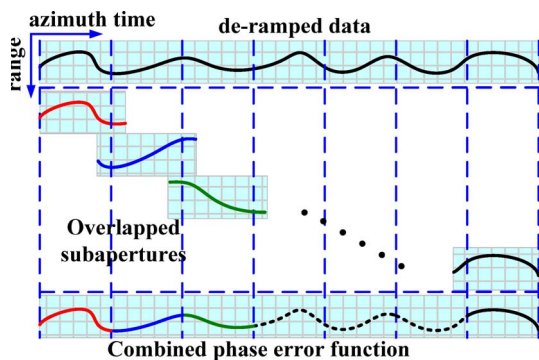


Fig. 10. Full-aperture phase error combination.

D. Full-Aperture Phase Combination

Similar to LML-PWE-PGA for the strip-map SAR autofocus, our approach also converts data blocks of the strip-map SAR into the spotlight representation. Each block is a segment of a full-aperture data. Although the windowing process is expected to avoid linear phase component in the PGA frameworks, small different linear phases exist in each phase error segment. Therefore, before we reconstruct the full-aperture functions of both range-invariant and variant phase errors, the involved linear phase differences should be removed appropriately. In the SAR imagery with subaperture process, overlapping is applied to avoid discontinuities between two joint subaperture blocks. In our approach, the overlapping segments also provide overlapping phase error estimates of the azimuth blocks, which are shown in Fig. 10. The linear phase differences can be easily extracted from the overlapping segments to reconstruct the phase errors for the full-aperture strip-map SAR data.

Similar to the conventional PGA approach, the LML-WPGA operates like a high-pass filter, and thus its precision degrades along with the increase in the clutter-phase perturbation, particularly when limited strong point targets exist in the scene. The phase error functions are affected by the high-frequency noise. Owing to the inertia of the UAV motion, the motion error should be smooth and continuous. Therefore, the combined phase error functions are smoothed to filter out the estimating noise. To implement this filter, autoregressive moving average has been applied [13]. Herein, we propose a simple but useful scheme. First, we set up the phase error function to be a high-order polynomial function with its order up to 10. The appropriate polynomial extracted the main low-frequency component of the phase function. The residual part was obtained by directly subtracting the polynomial function from the noisy function. In the second step, the useful information was retrieved from the residual phase, which corresponds to the medium frequency components. To distinguish the useful components from the noise, one can use some powerful transforms, such as the discrete cosine transform (DCT) [36] and the wavelet transform (WT) [37], [38]. By projecting the residual function into a frequency or time-frequency domain, only the useful large-valued and low-frequency components contained the information that we needed. Therefore, only the largest coefficients (usually eighth or quarter coefficients of the total number are good selections) were retained and the small ones were set as

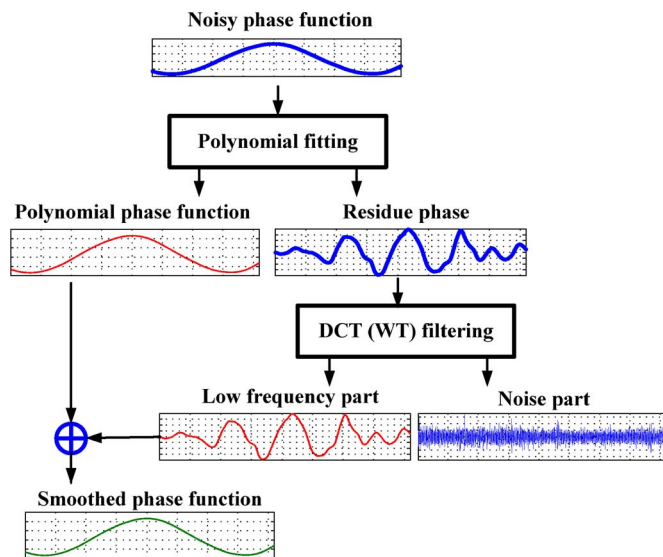


Fig. 11. Phase function filtering.

zeros. The inverse DCT or inverse WT was applied to obtain the required smoothed component. On summing up the smoothed part from the transform process and the polynomial function, one can achieve the de-noised phase function. Fig. 11 clearly illustrates this filtering process in detail.

E. Two-Step MOCO

After combining the subaperture phase errors (range-invariant phase errors and range-variant polynomial phase errors) into full-aperture functions, the MOCO for the full-aperture data was performed by a two-step scheme. In the first step, the range-invariant phase and the NRCM were corrected before range compression processing, and then the CSA was applied to complete the RCM correction and range compression. In the second step, the range-variant part of phase errors was calculated by the polynomial phase error functions to obtain a fine phase correction. Then, the azimuth compression was performed to generate the precisely focused UAV SAR image. The main flowchart of the MOCO process for the strip-map UAV SAR imagery is shown in Fig. 12. Our approach is different from some raw-database schemes [5], [13], and requires no process to estimate the motion errors iteration-by-iteration. Therefore, our approach has lower computational load than iterative approaches because both WPGA and LML-WPGA are implemented in a robust and efficient manner.

F. Extension to the Squinted SAR MOCO

In addition to the broadside-looking mode, the squint mode is important for the UAV SAR activities. In some cases, the antenna exhibits a pointing angle (called squint angle) offset from the zero Doppler direction, which is shown in Fig. 1 with $\alpha \neq 0$. Without losing generality, our MOCO should be adjusted to operate in a squint mode. In this section, we have introduced some modifications to the framework presented in Fig. 12 and extend it to the squint mode SAR imagery. The expression of instantaneous range from the scatterer to the

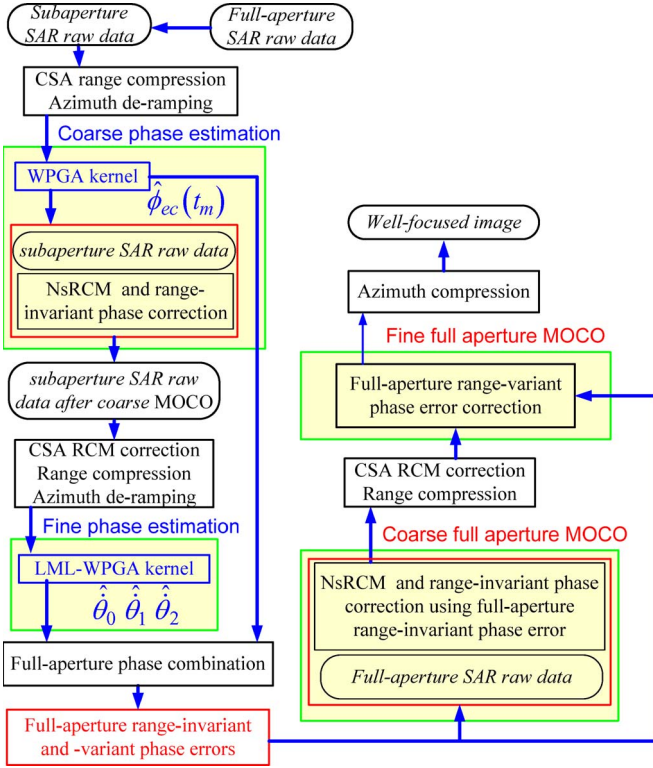


Fig. 12. Main flowchart of the proposed MOCO for strip-map UAV SAR imagery.

phase center (see (32), shown at the bottom of the page). Similar to (1), we split the range into two parts, and the second denotes the range error caused by trajectory deviations. The ideal range and error range are given by

$$R_b(t_m; r, x) = \sqrt{r^2 + (Vt_m - x)^2 - 2r(Vt_m - x) \sin \alpha} \quad (33)$$

$$\begin{aligned} \Delta R(t_m; x, y, z) &= R(t_m; r, x) - R_b(t_m; r, x) \\ &\approx \Delta R(t_m; r). \end{aligned} \quad (34)$$

In (34), the range error is simplified as range variant. In terms of developing an efficient and convenient image format, (33) is approximately equal to

$$\begin{aligned} R_b(t_m; r, x) &\approx \sqrt{r^2 + (\cos \alpha \cdot Vt_m - \cos \alpha \cdot x)^2} \\ &\quad - (Vt_m - x) \sin \alpha. \end{aligned} \quad (35)$$

Based on (35), a time domain range walk correction (RWC) can be used, which dramatically simplifies the imaging process for the squinted SAR [39], [40]. After RWC and range MF, the signal expression in the range frequency and azimuth time

domain is given in (36). For simplicity, the expression is still denoted by $s_r(f_r, t_m)$

$$\begin{aligned} s_r(f_r, t_m) &= \iint \sigma(x, r) \cdot g\left(t_m - \frac{x}{V}\right) \cdot s_t(f_r) \\ &\quad \cdot \exp\left[-j4\pi(f_c + f_r)\right. \\ &\quad \left. \times \frac{\sqrt{r^2 + (Vt_m \cos \alpha - x \cos \alpha)^2} + x \sin \alpha}{c}\right] \\ &\quad \cdot \exp\left[-j4\pi(f_c + f_r) \frac{\Delta R(t_m; r)}{c}\right] dr dx. \end{aligned} \quad (36)$$

After RCM correction by CSA, the range-compressed signal becomes

$$\begin{aligned} s_r(\hat{t}, t_m) &= \iint \sigma(x, r) \cdot g\left(t_m - \frac{x}{V}\right) \\ &\quad \cdot \text{sinc}\left[\gamma T_p \left(\hat{t} - \frac{2(r + x \sin \alpha + \Delta R(t_m; r))}{c}\right)\right] \\ &\quad \cdot \exp\left[-j4\pi f_c \frac{\sqrt{r^2 + (Vt_m \cos \alpha - x \cos \alpha)^2}}{c}\right] \\ &\quad \cdot \exp\left[-j4\pi f_c \frac{\Delta R(t_m; r)}{c}\right] dr dx. \end{aligned} \quad (37)$$

In the process of performing the CSA, the velocity is replaced by $V \cos \alpha$. Based on this signal model, our MOCO process can directly be applied in succession. The only difference is that the de-ramping reference function for the range bin at r is replaced by [40]

$$d(t_m) = \exp\left[j2\pi \frac{(\cos \alpha \cdot Vt_m)^2}{\lambda r}\right]. \quad (38)$$

We found that after the time-domain RWC, the signal DRs corresponding to targets confined in a range gate would differ from each other [39], [40]. This, obviously poses limitations on the MOCO scheme. Therefore, the focus depth or nonlinear chirp scaling should be considered in the application of MOCO to the high-squint SAR imagery [39].

V. REAL DATA EXPERIMENT

In the first experiment, the raw radar data with an imaging resolution of 0.75×0.75 m are collected by an experimental UAV-SAR, which was developed by the research institute of electronics technology in China. The UAV employed was ASN-206 in size of $3.8 \times 6 \times 1.4$ m (length \times width \times height)

$$\begin{aligned} R(t_m; r, x) &= \sqrt{(Vt_m + \Delta x(t_m) - x)^2 + (\Delta y(t_m) - y)^2 + (H + \Delta z(t_m) - z)^2} \\ &= R_b(t_m; r, x) + \Delta R(t_m; x, y, z) \end{aligned} \quad (32)$$

with a maximum carrying capacity of 40 kg. The experimental UAV-SAR system operated in X-band (9.5 GHz) with bandwidth 200 MHz. The slant range of the scene center was 12.9 km. The UAV flew at a height of about 3000 m, at a speed of 50–57 m/s. It was not equipped with highly accurate inertial navigation units and the navigation depended merely on a gyroscope and a GPS system. The altitude control was at an accuracy of 3 m, the gyroscope provided motion information at the frequency of 12.5 Hz, and its positioning accuracy of GPS was 30 m. Owing to the limitation and inaccuracy of the motion information, inertial navigation system (INS)-based MOCO was insufficient for the generation of the high quality imagery. Therefore, we needed a highly precise raw-data-based MOCO. The images with size (3072 × 2048 m, range × azimuth) generated by the INS-based MOCO and our approach are shown in Fig. 13(a) and (b), respectively. The vertical direction is azimuth, and the horizontal direction is range. Apparently, it can be noted that the image generated by the INS-based MOCO is seriously blurred and distorted in geometry due to the lack and inaccuracy of motion measurements. While the image achieved by our MOCO approach is focused with a high quality. In the MOCO process, the nominal trajectory was supposed at a height of 3000 m and with a constant velocity of 55 m/s. The raw data were segmented into 16 subapertures, and each of them was processed by the WPGA and LML-WPGA to retrieve the coarse and range-variant phase function, respectively. To highlight the severity of the UAV motion disturbance, the estimated coarse phase and the corresponding radial range error are shown in Fig. 14(a) and (b), respectively. Clearly, the range error is at an extent of $-1-4$ m, which exceeds about five range cells. Therefore, in addition, precise phase correction, a range migration correction is also necessary to obtain fully focused image. The range-invariant phase and range cell migration compensation implement the coarse MOCO in our approach. The range-variant phase correction is carried out to achieve a fine MOCO. The range-variant phase functions are estimated by the proposed LML-WPGA. In the LML-WPGA frame, the data were adaptively segmented into blocks in the range. The error phase functions, calculated by the polynomial estimate in the WPGA at six different range cells, are shown in Fig. 14(c), which present the spatial variance of the residual phase error after the coarse MOCO. By compensating the spatially variant phases, the UAV SAR imagery could be achieved with high precision. From Fig. 13(b), one can see the towns, rivers, freeway, villages, and wild scenes clearly distinguished and well focused. The local scene, highlighted in Fig. 13(b) by white circle, is amplified in Fig. 13(d). There are three groups of corner reflectors array. Each array is composed of five metal corner reflectors as a cross with a space of 2.5 m between two arrays. As clearly presented in Fig. 13(d), the corner reflector arrays are focused in an ideal way. To show the superiorities of the proposed algorithm, we also performed the MOCO by using the DR-based MOCO [5]. The DR-based method is an effective candidate to the airborne SAR MOCO. It extracts motion errors from raw data by MD algorithm in an iterative manner. In each iteration, full-aperture data are first compensated by motion information extracted from the last iteration, and then it is divided into small blocks in both range and azimuth to

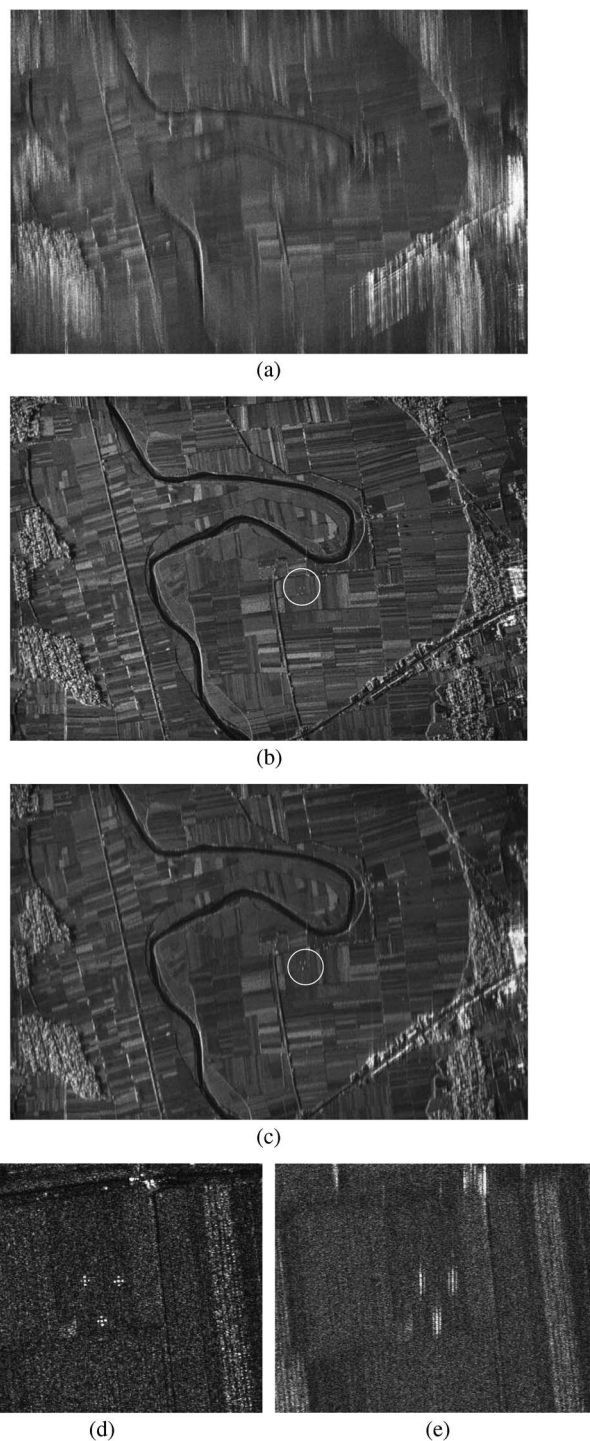


Fig. 13. UAV SAR images. (a) With INS-based MOCO. (b) With the proposed MOCO. (c) With the DR-based MOCO. (d) Corner reflectors array circled in Fig. 13(b). (e) Corner reflectors array circled in Fig. 13(c).

perform DR estimation. Finally, the DRs are linearly fitted and interpolated to obtain the motion parameters. Generally, to retrieve accurate motion error for UAV SAR MOCO, this iteration is repeated many times before it reaches an optimal convergence, bringing large computational burden. However, in the proposed method, the motion errors are just divided into range-variant and invariant parts, which are precisely estimated by the WPGA and LML-WPGA. Owing to the high efficiency

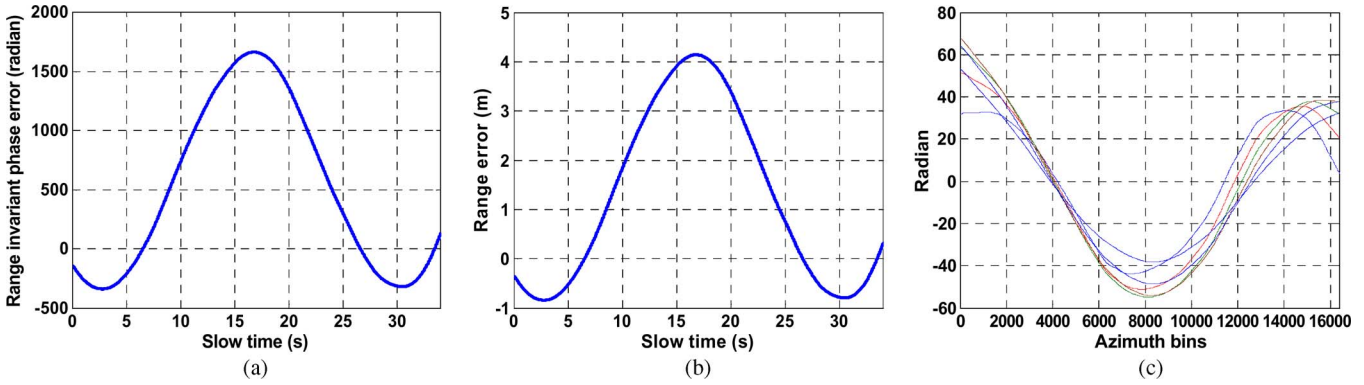


Fig. 14. Phase error and range error. (a) Range-invariant phase error function. (b) Corresponding radial range error function. (c) Residual phase errors at different range bins.

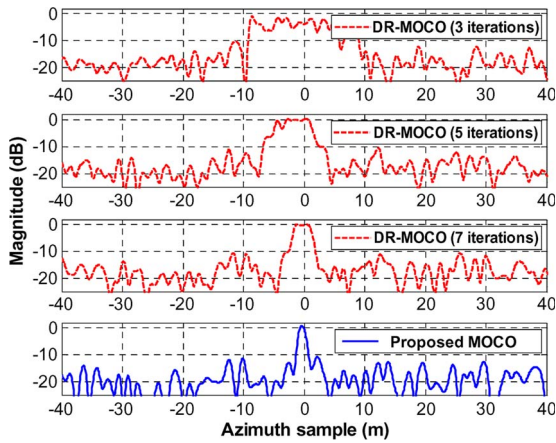


Fig. 15. Response functions of a corner reflector by the DR-based and proposed MOCO.

of WPGA and LML-WPGA, the MOCO is performed much easily. For comparison, the image, obtained by the DR-based MOCO with three iterations, is provided in Fig. 13(c). In the DR estimation, the data are divided into 24×70 (range \times azimuth) sub-blocks. Clearly, with three iterations, the DR-based method removes majority of the motion errors and generates a coarse-focused image. However, the residual error is still significant enough to cause serious blurring, which can be found in the corner reflector array shown in Fig. 13(e). With increasing the iteration number, the motion error was corrected gradually. However, the computational load was increased proportionally. The DR-based method with three iterations took 3 h and 27 min. However, the proposed method spent only 38 min to correct both the range-invariant and variant phase errors accurately. Notably, the proposed MOCO is more efficient than the DR-based one. To demonstrate this, we have provided the impulse response functions of one corner reflector corresponding to the DR-based method with 3, 5, 7 iterations and the proposed method in Fig. 15. One can find that only the proposed method generates ideal response with a resolution of 0.761 m, while the resolution achieved by the DR-based method with seven iterations is still up to 2.33 m. Owing to the severe clutter turbulence, peak-to-sidelobe ratio generated by the proposed method is up to -12.2 dB. This result shows that the proposed method possesses both efficiency and precision. This experiment confirms that our MOCO approach is robust and efficient

with respect to the strip-map UAV SAR imagery and should be suitable for the UAV SAR MOCO in real time.

In the following, we have presented the experimental results of the UAV SAR imagery operating in a squint mode. It provides a resolution of 2.15×2.15 m (range \times azimuth). The squint angle is about 55° and the flying velocity is about 60 m/s. The height of the UAV is about 2800 m, and the range central to the scene is 2.832 km. The experimental SAR system is kept identical to that employed in the former experiment apart from the use of a low-accuracy INS. The SAR image has been obtained by using the recorded motion parameters from the INS, as shown in Fig. 16(a). In Fig. 16(b), the image generated by applying the proposed MOCO approach after the time-domain RCW, is presented. The vertical direction is range, and the horizontal direction is azimuth. In comparison, the magnified images of the circled scene in Fig. 16(a) and (b) are shown in Fig. 16(c) and (d), respectively. Obviously, the image generated by the INS data MOCO is seriously blurred and distorted due to the inaccuracy of motion recording. However, the image generated by the proposed MOCO is well-focused. This experiment validates our method for the squint-mode UAV SAR imagery.

VI. CONCLUSION

In this paper, a robust and efficient MOCO for the UAV SAR imaging has been proposed. The approach first estimates range-invariant phase error by the robust WPGA, which is applied to correct NRCM and error phases of implementing a coarse MOCO step. Second, an LML-WPGA kernel has been developed to retrieve the residual phase errors. In the LML-WPGA estimate, the range-variant phase error is modeled as a polynomial function of range. Then, the range-variant phase error is precisely obtained by an LML estimation of phase gradient for each range block. It has been found that the WPGA technique and LML estimation of phase gradient lead to a robust and efficient MOCO for the UAV SAR imagery. Both the simulated and real UAV SAR data experiments show that the proposed approach is appropriate for the low-altitude UAV SAR systems equipped with a low-accuracy navigation system. Furthermore, the LML has been extended to the current PWE-PGA and WPCA algorithms, and promising improvement in both precision and efficiency has been achieved.

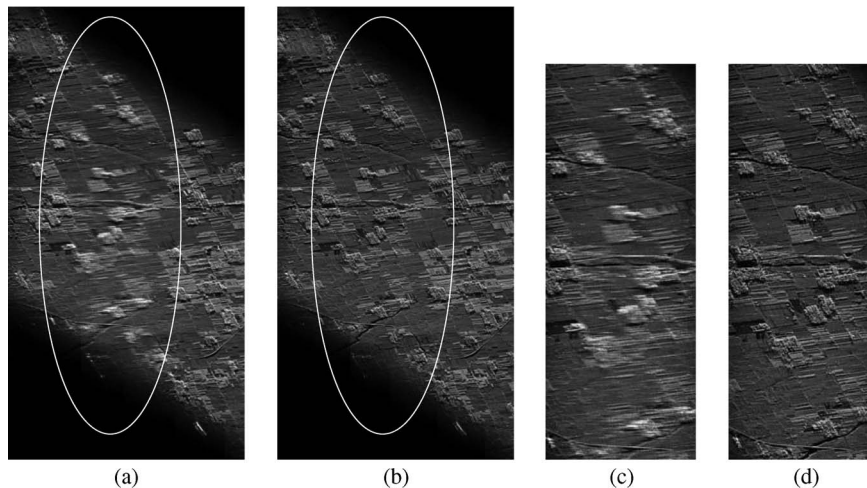


Fig. 16. Squint-mode experimental results. (a) MOCO with INS information. (b) MOCO with the proposal. (c) Magnified image circled in (a). (d) Magnified image circled in (b).

ACKNOWLEDGMENT

The authors thank the anonymous reviewers for their valuable comments to improve the paper's quality.

REFERENCES

- [1] W. G. Carrara, R. S. Goodman, and R. M. Majewski, *Spotlight Synthetic Aperture Radar: Signal Processing Algorithm*. Boston, MA: Artech House, 1995.
- [2] G. Fornaro, "Trajectory deviations in airborne SAR: Analysis and compensation," *IEEE Trans. Aerosp. Electron. Syst.*, vol. 35, no. 3, pp. 997–1009, Jul. 1999.
- [3] A. Moreira and H. Yonghong, "Airborne SAR processing of highly squinted data using a chirp scaling approach with integrated motion compensation," *IEEE Trans. Geosci. Remote Sens.*, vol. 32, no. 5, pp. 1029–1040, Sep. 1994.
- [4] W. Wang, Q. Peng, and J. Cai, "Waveform-diversity-based millimeter-wave UAV SAR remote sensing," *IEEE Trans. Geosci. Remote Sens.*, vol. 47, no. 3, pp. 691–700, Mar. 2009.
- [5] M. Xing, X. Jiang, R. Wu, F. Zhou, and Z. Bao, "Motion compensation for UAV SAR based on raw radar data," *IEEE Trans. Geosci. Remote Sens.*, vol. 47, no. 8, pp. 2870–2883, Aug. 2009.
- [6] C. Oliver and S. Quegan, *Understanding Synthetic Aperture Radar Images*. Norwood, MA: Artech House, 1999.
- [7] G. Franceschetti and R. Lanari, *Synthetic Aperture Radar Processing*. Boca Raton, FL: CRC Press, 1999.
- [8] P. Samczyński, G. Pietrzyk, and A. Gorzelanczyk, "Coherent MapDrift technique," *IEEE Trans. Geosci. Remote Sens.*, vol. 48, no. 3, pp. 1505–1517, Mar. 2010.
- [9] J. T. Gonzalez Partida, P. Almorox Gonzalez, and M. Burgos Garcia, "SAR system for UAV operation with motion error compensation beyond the resolution cell," *Sensors*, vol. 8, no. 5, pp. 3384–3405, May 2008.
- [10] D. E. Wahl, P. H. Eichel, D. C. Ghiglia, and C. V. Jakowatz, Jr., "Phase gradient autofocus—A robust tool for high resolution phase correction," *IEEE Trans. Aerosp. Electron. Syst.*, vol. 30, no. 3, pp. 827–835, Jul. 1994.
- [11] H. L. Chan and T. S. Yeo, "Noniterative quality phase-gradient autofocus (QPGA) algorithm for spotlight SAR imagery," *IEEE Trans. Geosci. Remote Sens.*, vol. 36, no. 5, pp. 1531–1539, Sep. 1998.
- [12] W. Ye, T. S. Yeo, and Z. Bao, "Weighted least-squares estimation of phase errors for SAR/ISAR autofocus," *IEEE Trans. Geosci. Remote Sens.*, vol. 37, no. 5, pp. 2487–2494, Sep. 1999.
- [13] K. A. C. de Macedo, R. Scheiber, and A. Moreira, "An autofocus approach for residual motion errors with application to airborne repeat-pass SAR interferometry," *IEEE Trans. Geosci. Remote Sens.*, vol. 46, no. 10, pp. 3151–3162, Oct. 2008.
- [14] P. Prats, K. A. Câmara de Macedo, A. Reigber, R. Scheiber, and J. J. Mallorqui, "Comparison of topography- and aperture-dependent motion compensation algorithms for airborne SAR," *IEEE Geosci. Remote Sens. Lett.*, vol. 4, no. 3, pp. 349–353, Jul. 2007.
- [15] Cumming, J. R. Bennett, and R. A. Deane, "The digital processing of SEASAT SAR data," in *Proc. IEEE Int. Radar Conf.*, 1980, pp. 710–718.
- [16] M. Y. Lin and C. Wu, "A SAR correlation algorithm which accommodates large range migration," *IEEE Trans. Geosci. Remote Sens.*, vol. GRS-22, no. 6, pp. 592–597, Nov. 1984.
- [17] J. L. Walker, "Range-Doppler imaging of rotating objects," *IEEE Trans. Aerosp. Electron. Syst.*, vol. AES-16, no. 1, pp. 23–52, Jan. 1980.
- [18] R. K. Raney, H. Runge, R. Bamler, I. G. Cumming, and F. H. Wong, "Precision SAR processing using chirp scaling," *IEEE Trans. Geosci. Remote Sens.*, vol. 32, no. 4, pp. 786–799, Jul. 1994.
- [19] F. Wong, I. Cumming, and R. K. Ranley, "Processing simulated RADARSAT SAR data with squint by a high precision algorithm," in *Proc. IEEE Geosci. Remote Sens. Symp.*, 1993, pp. 1176–1178.
- [20] G. W. Davidson, "A chirp scaling approach for processing high squint mode SAR data," *IEEE Trans. Aerosp. Electron. Syst.*, vol. 32, no. 1, pp. 121–133, Jan. 1996.
- [21] J. Mittermayer, A. Moreira, and O. Loffeld, "Spotlight SAR data processing using the frequency scaling algorithm," *IEEE Trans. Geosci. Remote Sens.*, vol. 37, no. 5, pp. 2198–2214, Sep. 1999.
- [22] I. Cumming and F. Wang, *Digital Processing of Synthetic Aperture Radar Data: Algorithm and Implementation*. Norwood, MA: Artech House, 2005.
- [23] D. E. Wahl, C. V. Jakowatz, Jr., P. A. Thompson, and D. C. Ghiglia, "New approach to strip-map SAR autofocus," in *Proc. 6th IEEE Digit. Signal Process. Workshop*, Yosemite National Park, CA, Oct. 1994, pp. 53–56.
- [24] J. H. Callow, "Signal processing for synthetic aperture sonar image enhancement," Ph.D. dissertation, Dept. Elect. Electron. Eng., Univ. Canterbury, Christchurch, New Zealand, 2003.
- [25] M. P. Hayes, H. J. Callow, and P. T. Gough, "Stripmap phase gradient autofocus," in *Proc. OCEANS*, Sep. 22–26, 2003, vol. 5, pp. 2414–2421.
- [26] P. T. Gough, M. P. Hayes, and D. R. Griffiths, "Strip-map path correction using phase matching autofocus," in *Proc. 5th ECUA*, Lyon, France, Jul. 2000, pp. 412–418.
- [27] S. N. Madsen, "Estimating the Doppler centroid of SAR data," *IEEE Trans. Aerosp. Electron. Syst.*, vol. 25, no. 2, pp. 134–140, Mar. 1989.
- [28] F. H. Wang and I. G. Cumming, "A combined SAR Doppler centroid estimation scheme based upon signal phase," *IEEE Trans. Geosci. Remote Sens.*, vol. 34, no. 3, pp. 696–707, May 1996.
- [29] I. G. Dimming, "A spatially selective approach to Doppler estimation for frame-based satellite SAR processing," *IEEE Trans. Geosci. Remote Sens.*, vol. 42, no. 6, pp. 1135–1148, Jun. 1996.
- [30] D. G. Thompson, J. S. Bates, D. V. Arnold, and D. G. Long, "Extending the phase gradient autofocus algorithm for low-altitude stripmap mode SAR," in *Proc. IGARSS*, Hamburg, Germany, Jul. 1999, pp. 564–566.
- [31] A. W. Doerry, "Autofocus correction of excessive migration in synthetic aperture radar images," Sandia Nat. Lab., Albuquerque, NM, Sandia Rep. SAND2004-4770, Sep. 2004.
- [32] G. Fornaro, G. Franceschetti, and S. Perna, "On center-beam approximation in SAR motion compensation," *IEEE Trans. Geosci. Remote Sens.*, vol. 3, no. 2, pp. 276–280, Apr. 2006.
- [33] P. Prats, A. Reigber, and J. J. Mallorqui, "Topography-dependent motion compensation for repeat-pass interferometric SAR systems," *IEEE Geosci. Remote Sens. Lett.*, vol. 2, no. 2, pp. 206–210, Apr. 2005.
- [34] K. A. C. de Macedo and R. Scheiber, "Precise topography- and aperture-dependent motion compensation for airborne SAR," *IEEE Geosci. Remote Sens. Lett.*, vol. 2, no. 2, pp. 172–176, Apr. 2005.

- [35] R. Scheiber and V. Bothale, "Interferometric multi-look techniques for SAR data," in *Proc. IEEE IGARSS*, Toronto, ON, Canada, Jun. 24–28, 2002, vol. 1, pp. 173–175.
- [36] N. Ahmed, T. Natarajan, and K. R. Rao, "Discrete cosine transform," *IEEE Trans. Comput.*, vol. C-23, no. 1, pp. 90–93, Jan. 1974.
- [37] S. Mallat, "A theory for multiresolution signal decomposition: The wavelet representation," *IEEE Trans. Pattern Anal. Mach. Intell.*, vol. 11, no. 7, pp. 674–693, Jul. 1989.
- [38] D. L. Donoho and I. M. Johnstone, "Adapting to unknown smoothness via wavelet shrinkage," *J. Amer. Stat. Assoc.*, vol. 90, no. 432, pp. 1200–1224, Dec. 1995.
- [39] F. H. Wong and T. S. Yeo, "New applications of non-linear chirp scaling in SAR data processing," *IEEE Trans. Geosci. Remote Sens.*, vol. 39, no. 5, pp. 946–953, May 2001.
- [40] T. S. Yeo, N. L. Tan, C. B. Zhang, and Y. H. Lu, "A new subaperture approach to high squint SAR processing," *IEEE Trans. Geosci. Remote Sens.*, vol. 39, no. 5, pp. 954–968, May 2001.



Meng-dao Xing (M'04) was born in Zhejiang, China, in November, 1975. He received the Bachelor and Ph.D degrees in electrical engineering from Xidian University, Xi'an, China, in 1997 and 2002, respectively.

He is currently a Full Professor with the National Key Laboratory for Radar Signal Processing, Xidian University. His research interests include SAR, ISAR, and over-the-horizon radar.



Lei Zhang was born in Zhejiang Province, China, 1984. He received the B.S. degree in mechanism and electrical engineering from Chang'an University, Xi'an, China, in 2006. He is currently working toward the Ph.D degree in signal processing at the National Key Lab of Radar Signal Processing of Xidian University, Xi'an.

His major research interests are SAR/ISAR.



Lei Yang was born in Tianjing City, China, in 1984. He received the B.S. degree in electrical engineering from Xidian University, Xi'an, China, in 2007, where he is currently working toward the Ph.D degree in signal processing at the National Key Lab of Radar Signal Processing.

His major research interests are radar imaging and motion compensation.



Zhijun Qiao (M'10) received the Ph.D. degree in applied math from the Institute of Mathematics, Fudan University, Shanghai, China, in 1997, where his dissertation was one of the first 100 excellent Ph.D. dissertations awarded in 1999.

From 1999 to 2001, he was a Humboldt Research Fellow with the Department of Mathematics and Computer Science, University of Kassel, Germany. From 2001 to 2004, he was a Researcher with the Theoretical Division, Los Alamos National Laboratory. He was also a Professor with the Department

of Mathematics, Liaoning University, Shenyang City, China, since 1997. Currently, he is the Principal Investigator of two grants under the Department of Defense program and the Norman Hackerman Advanced Research Program. He is currently with the Department of Mathematics, The University of Texas-Pan American, Edinburg. He is currently the Editor-in-Chief of the *Pacific Journal of Applied Mathematics*. He has published two monographs and more than 90 articles in peer-reviewed international journals. His research interest includes nonlinear partial differential equations and its application in radar imaging.



Zheng Bao (M'80–SM'90) was born in Jiangsu, China. He received the B.S. degree from the Communication Engineering Institute of China (currently, Xidian University), Xi'an, China, in 1953.

Currently, he is a Professor with Xidian University and the Chairman of the academic board of the National Key Lab of Radar signal Processing. He has authored or coauthored six books and published over 300 papers. Now, his research fields include space-time adaptive processing, radar imaging (SAR/ISAR), automatic target recognition, and over-

the-horizon radar signal processing.

Prof. Bao is a member of the Chinese Academy of Sciences.